Element specific atom counting for heterogeneous nanostructures : combining multiple ADF STEM images for simultaneous thickness and composition determination

Element specific atom counting for heterogeneous nanostructures: Combining multiple ADF STEM images for simultaneous thickness and composition determination

D.G. Şentürk[a,b,1], A. De Backer[a,b,1], S. Van Aert[a,b,*]

[a] *Electron Microscopy for Materials Science (EMAT), University of Antwerp, Groenenborgerlaan 171, 2020 Antwerp, Belgium*
[b] *NANOlab Center of Excellence, University of Antwerp, Groenenborgerlaan 171, 2020 Antwerp, Belgium*

Abstract

In this paper, a methodology is presented to count the number of atoms in heterogeneous nanoparticles based on the combination of multiple annular dark field scanning transmission electron microscopy (ADF STEM) images. The different non-overlapping annular detector collection regions are selected based on the principles of optimal statistical experiment design for the atom-counting problem. To count the number of atoms, the total intensities of scattered electrons for each atomic column, the so-called scattering cross-sections, are simultaneously compared with simulated library values for the different detector regions by minimising the squared differences. The performance of the method is evaluated for simulated Ni@Pt and Au@Ag core-shell nanoparticles. Our approach turns out to be a dose efficient alternative for the investigation of beam-sensitive heterogeneous materials as compared to the combination of ADF STEM and energy dispersive X-ray spectroscopy.

1. Introduction

Nanoparticles have become increasingly important in diverse research fields, including biosensing, wastewater treatment and catalysis owing to their unique properties [1–6]. Among the different types of nanoparticles, multimetallic core-shell nanoparticles have gathered considerable attention in recent years [7–12]. These nanoparticles consist of a metallic core coated by a shell composed of a different metal or alloy, allowing to utilise the unique characteristics of each element or their specific combination. By mixing different metals, the nanoparticles exhibit enhanced and adjustable magnetic, optical and catalytic properties that are modifiable through variations in their composition, core size and shell thickness [4, 5, 13–16].

To fully understand the properties of these nanoparticles, precise structural characterisation of their atomic composition is crucial. Scanning transmission electron microscopy (STEM) can play an important role here. More specific, atomic resolution high-angle annular dark field (HAADF) STEM imaging, known for its ability to detect both thickness and elemental composition, is widely recognised as a well-suited technique for nanostructure characterisation [17].

Counting the number of atoms from such ADF STEM images has proven useful for determining the precise arrangement of all atoms in 3D for monometallic nanocrystals [18–22]. However, a simultaneous quantification of both composition and thickness in an atomic column is not a straightforward task due to the diverse types of elements and their various 3D arrangements contributing differently to the image intensities. In literature, several methodologies have been proposed to count the number of each type of atoms within multimetallic nanoparticles from a single ADF STEM image by direct comparison of normalised experimental image with simulated intensities [23, 24]. These approaches benefit from either prior knowledge about the shape of the nanoparticle or the determination of atomic column composition through the utilisation of thickness information from the nearest neighbouring columns. However, prior knowledge is not always available. Consequently, there is a need for a methodology that can be applied to nanostructures with varying neighbouring column compositions without relying on prior knowledge of the nanoparticle's structure. To address this challenge, a recent study demonstrated the benefit of combining elemental composition information from EDX signals with a HAADF STEM image to simultaneously determine the composition and thickness of core-shell type nanostructures such as Au@Ag and Au@Pt [25]. However, when it comes to beam-sensitive materials, the use of EDX measurements may not always be the most viable option due to the significant electron dose needed to achieve a sufficiently high signal-to-noise ratio in the EDX elemental maps. An alternative approach to simultaneously reveal thickness and composition information is through employing multimode atomic resolution ADF STEM [26–28]. In this technique, distinct scattering behaviours in different annular detector collection regions help to unscramble the composition and thickness. For this purpose, optimal detector settings can be derived that yield the most precise quantification of the structure parameters [29]. Here, we present a simulation study that illustrates the practical application of element-specific atom counting for bimetallic core-shell nanoparticles, based on an optimal set of multiple ADF STEM images. The method relies on the comparison of simulated atom column intensities with normalised experimentally measured atom column intensities.

The paper is structured as follows: Section 2 provides a de-

*Corresponding author
[1] Both authors contributed equally to this work.

tailed explanation of the methodology for element-specific atom counting based on the combination of multiple ADF STEM images. In Section 3, we introduce the exploratory case studies and simulation parameters. Section 4 presents the proof of concept through comprehensive simulations conducted for three different types of spherical core-shell nanoparticles. Here, we discuss the performance of our methodology considering variations in the atomic number of elements and the size of nanoparticles. Finally, in Section 5, we offer general discussions and draw conclusions based on our findings.

2. Methodology

To collect a combination of ADF STEM images for multiple detector regions, the 4D STEM technique with a pixelated detector is highly advantageous. It enables to obtain multiple virtual STEM images belonging to arbitrary annular detector angles without the need for pre-configured instrumental settings [30–34]. When comparing these experimental images with reference image simulations, the experimental images will be normalised with respect to the number of incident electrons [34–44]. To count the number of atoms, the column intensities should be quantified. For this purpose, the so-called scattering cross-sections is used which is defined as the total intensity of electrons of each atomic column scattered toward the ADF detector [45, 46]. The scattering cross-section offers advantages over the peak intensity given its sensitivity to the number and type of atoms and its robustness to experimental parameters such as defocus, source size broadening, and slight sample mistilt [47, 48]. The scattering cross-sections can be computed either by using Voronoi cells [20, 49] or by estimating the volume of Gaussian functions which are fitted to the atomic columns in the image [45, 50, 51]. For the latter, the image is modelled as a superposition of Gaussian functions which are peaked at the atomic column positions from which the unknown parameters are estimated by minimising the least-squares sum [45, 52]. Example maps of estimated scattering cross-sections of a core-shell nanoparticle, denoted as $(SCS_n^{\exp_1}, SCS_n^{\exp_2})$ with n the atomic column index, for two virtual ADF STEM images with detector angles equal to 21-27 mrad and 27-170 mrad are presented in Fig. 1(a). The nanoparticle's scattering cross-section values are then compared with reference unit cell simulations.

This library is constructed from unit cell simulations where each supercell contains identical atomic columns. Given that the total thickness of the nanoparticle is unknown, a reasonable approach is to consider a wide range of thicknesses. Considering all possible 3D arrangements of two element types in the atomic column would require a large number of simulations. Therefore, the number of simulations is limited through assumptions about the nanostructure's type, such as whether the atoms in the atomic column are arranged in a core-shell or alloy-type configuration. It is worth noting that a prior study has indicated that the depth location of a single atomic column does not significantly change the scattering cross-section [29, 53]. Hence, in the case of core-shell type atomic column compositions, simplifying the atomic column type assumptions by placing the core in the centre of the atomic column would be an acceptable strategy for determining the elemental counts. The scattering cross-sections computed from the unit cell simulations for the different atomic arrangements are illustrated in Fig. 1(b).

By matching the nanoparticle scattering cross-sections (experimental) and the unit cell scattering cross-sections (simulated), the number and type of atoms can be assigned for each atomic column. In practice, this can be done by minimising the uniformly weighted sum of squared differences in the scattering cross-sections from the multiple images. This approach can be formulated as follows:

$$\hat{m}_n = \arg\min_m \sum_{d=1}^{D} (SCS_n^{exp_d} - SCS_m^{sim_d})^2. \quad (1)$$

In this expression, n is the atomic column index, d refers to the detector region for D detectors, $SCS_n^{exp_d}$ is the nanoparticle's scattering cross-section of the nth atomic column obtained from the dth ADF STEM image, and $SCS_m^{sim_d}$ is the simulated unit cell scattering cross-section for the mth configuration with a specific thickness and composition. The least squares sum is minimised and provides the estimated configuration $\hat{m}_n$ for the nth atomic column.

To better understand the benefit of combining scattering cross-sections from multiple detector regions, an example for two arbitrary columns is illustrated in Fig. 1(b). The black arrows indicate two scattering cross-section values that cannot be distinguished by using the information provided from the first annular detector region only. This hampers a correct assignment of the thickness and composition for such a scattering cross-section value. For the second detector, the scattering cross-sections of these two column configurations differ. Other columns will possess the opposite characteristic, i.e. the scattering cross-sections will be different for the first detector and similar for the second detector. In this manner, the combination of two detectors enables a unique assignment of the composition and thickness for all atomic columns. To validate this concept and investigate the precision and accuracy of the presented methodology, this approach will be applied to simulations of different spherical bimetallic core-shell nanoparticles.

3. Simulation settings

The details of the simulations for the studied nanoparticles are given in this section. The three bimetallic spherical nanoparticle structures, illustrated in Fig. 2, are:

1. *A spherical Ni@Pt core-shell nanoparticle* with a diameter of 6 nm as shown in Fig. 2(a). The pink-coloured atoms represent the Ni atoms at the core and the blue-coloured atoms illustrate the Pt atoms located on the shell. Both pure Pt and mixed Pt-Ni atomic columns are present in this structure. The number of atoms in the atomic columns along the [110] projection direction varies from 1 up to 22 atoms for the total number of atoms, from 2 up to 15 atoms for the number of Ni atoms in the core, and from 1

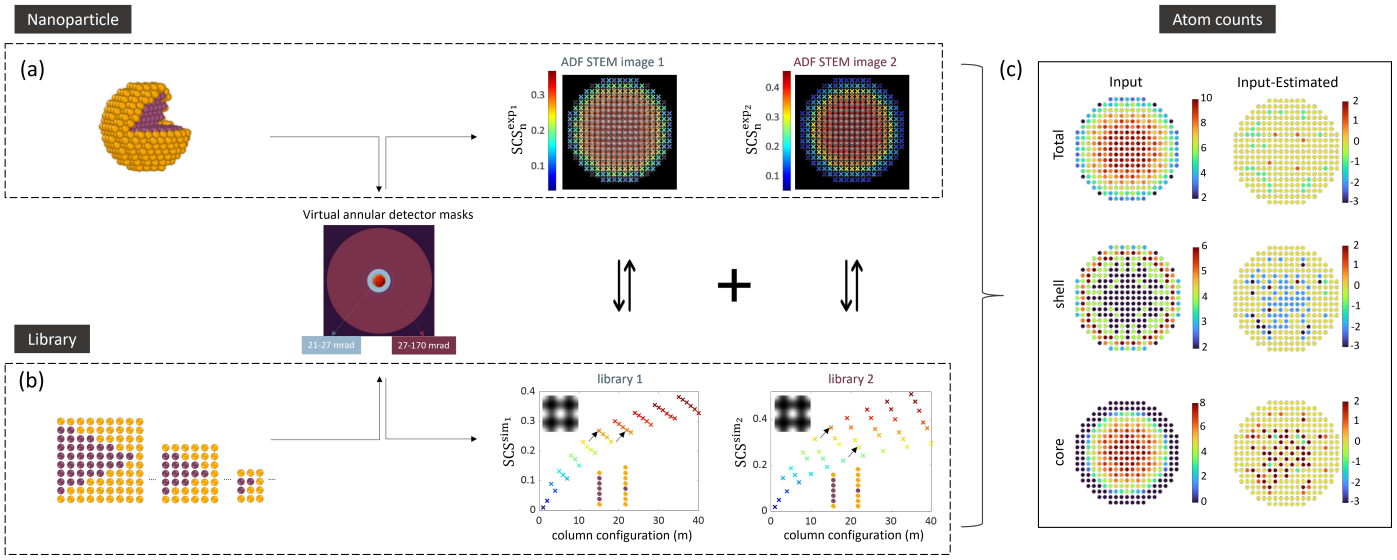

Figure 1: Illustration for element-specific atom counting methodology. (a) A bimetallic spherical core-shell nanoparticle and two virtual ADF STEM images together with the measured scattering cross-sections for each atomic columns. (b) The configuration of simulated library atomic columns with varying thickness and chemical composition and the corresponding library of scattering cross-sections evaluated from the unit cell simulations. The library scattering cross-section values are illustrated with the same color code as the scattering cross-sections in (a). (c) The estimated total number of atoms, number of atoms for the type of element located at core and the number of atoms located at shell part of the nanoparticle.

up to 16 atoms for the number of Pt atoms in the shell of nanoparticle. To estimate the number and type of atoms in this nanoparticle, 465 different atomic column configurations are constructed as a library consisting of both mono-type Pt atomic columns and core-shell ordered mixed-type atomic columns where the Ni atoms are located at the centre of columns. The thickness of the atomic columns of the library varies from 1 up to 30 atoms.

2. *A spherical Au@Ag core-shell nanoparticle* with a diameter of 6 nm as shown in Fig. 2(b). The yellow-coloured atoms represent the Au atoms at the core and the gray-coloured atoms show the Ag atoms of the shell. Also here, both pure Ag and mixed Ag-Au atomic columns are present in this structure. The number of atoms in the atomic columns along the [110] projection direction varies from 1 up to 21 atoms for the total number of atoms, from 2 up to 16 atoms for the number of Au atoms in the core, and from 1 up to 15 atoms for the number of Ag atoms in the shell of the nanoparticle. The library is constructed in the same manner as explained for the Ni@Pt nanoparticle.
3. *A larger spherical Au@Ag core-shell nanoparticle* with a diameter of 21 nm. A cross-section of this structure is shown in Fig. 2(c). For computational efficiency, only a small part of the nanoparticle is investigated which is indicated by the red box in the figure. This part contains pure Ag and mixed Ag-Au atomic columns. The number of atoms in the atomic columns along the [110] projection direction of the selected part varies from 60 up to 76 atoms for the total number of atoms, from 3 up to 36 atoms for the number of Au atoms in the core, and from 40 up to 67 atoms for the number of Ag atoms in the shell. To estimate the number and type of atoms in this nanoparticle, 2096 different atomic columns are constructed as a library consisting of mono-type Ag atomic columns and core-shell ordered mixed-type atomic columns where the Au atoms are located in the middle of columns. The thickness of the atomic columns of the library varies from 50 up to 81 atoms.

For the three nanostructures, 4D STEM datasets are generated by using the MULTEM software [54]. The parameters of the multislice simulation using the frozen-phonon approximation are listed in Table 1. The Debye-Waller B factors for each element in the three nanoparticles are selected based on the parametric values derived by Gao and Peng [55].
In this study, both the combination of two and three ADF STEM images are investigated to perform atom-counting for the described nanoparticles. For each of the structures, we first derived the optimal settings for the combination of multiple non-overlapping annular detector collection regimes. Following the approach of Şentürk et al. [29], the optimal settings result in estimates of the number and type of atoms with the highest accuracy. The optimal settings are derived based on the scattering cross-sections measured from the library simulations for the different atomic columns. The details of this analysis by using the probability of error are provided in Appendix A. The optimal detector settings are summarised in Table 2 according to the results provided in Fig. A.1(a)-(c). It should be noted that contributions of diffuse scattering originating from static atomic displacements in multi-element nanostructures and inelastic plasmon excitations are not taken into account in the simulations [26, 41, 42, 49, 56–59]. In this study, the exclusion of these factors is not expected to impact the results significantly, as the emphasis is on comparing simulated datasets. For

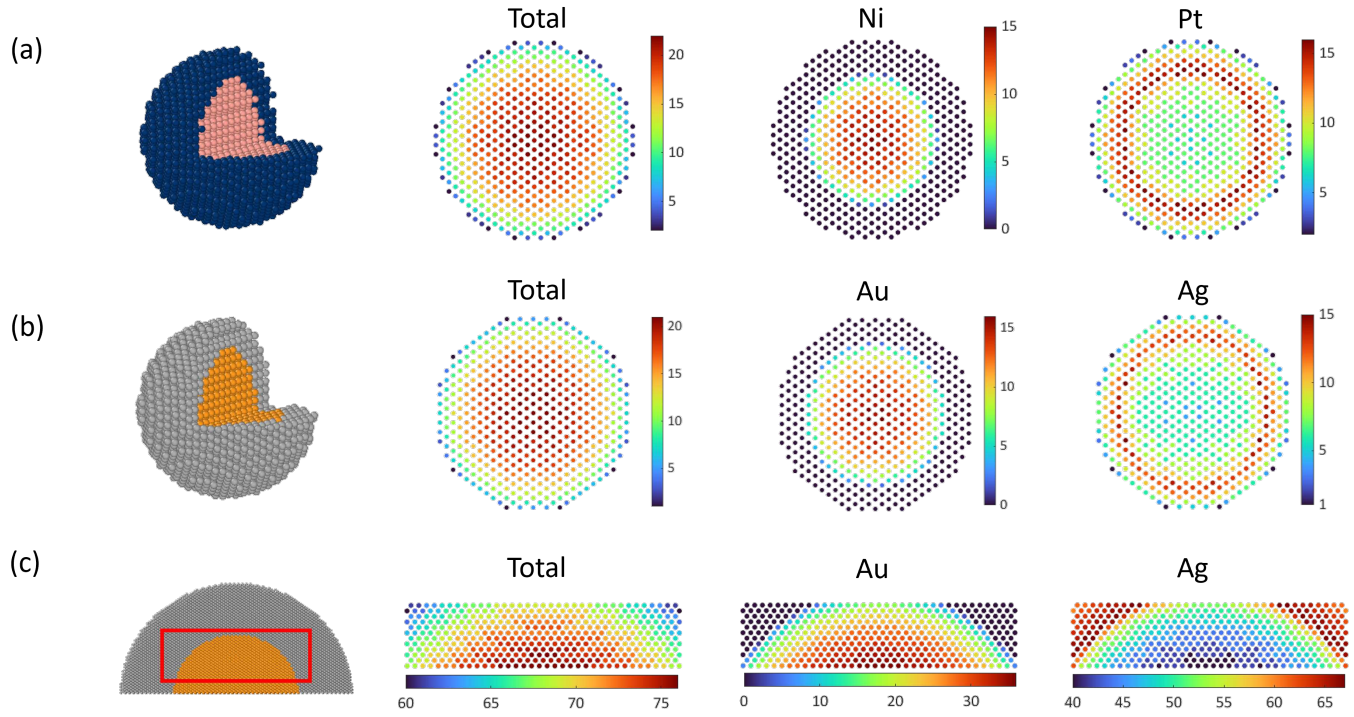

Figure 2: Illustration of the three bimetallic spherical nanoparticle case studies with number of atoms at each atomic column. (a) Ni@Pt core-shell nanoparticle with varying thickness from 1 up to 21 atoms, (b) Au@Ag core-shell nanoparticle with varying thickness from 1 up to 22 atoms and (c) cross-section of a Au@Ag core-shell nanoparticle with varying thickness from 1 up to 77 atoms. The area inside the red box illustrates the investigated region where total thickness varies from 60 up to 76 atoms.

Parameter	Value
Zone axis orientation	[110]
Acceleration voltage	300 kV
Defocus	-17.184 Å
Spherical aberration	0.001 mm
Semi-convergence angle	20 mrad
Number of phonon configurations	30
Maximal outer detector angle	170 mrad
FWHM of the source image	1.4 Å
Debye-Waller B factor:	
Au	0.637 $Å^2$
Ag	0.761 $Å^2$
Pt	0.384 $Å^2$
Ni	0.378 $Å^2$
Probe sampling distance:	
NPs STEM	0.1805 Å
Ni@Pt UC STEM	0.1453 Å
Au@Ag UC STEM	0.1510 Å
Simulation box size:	
Ni@Pt NP (6 nm)	6.9×6.9 nm^2
Au@Ag NP (6 nm)	6.9×6.9 nm^2
Au@Ag NP (21 nm)	14.7×14.7 nm^2
Ni@Pt UCs	2.7×2.7 nm^2
Au@Ag UCs	2.8×2.8 nm^2
Total number of scanned pixels:	
Ni@Pt NP (6 nm)	363×366
Au@Ag NP (6 nm)	363×366
Au@Ag NP (21 nm)	603×179
UC simulations	27×19
Pixel size in reciprocal space:	
Ni@Pt NP (6 nm)	0.0145 $Å^{-1}$
Au@Ag NP (6 nm)	0.0145 $Å^{-1}$
Au@Ag NP (21 nm)	0.0068 $Å^{-1}$
Ni@Pt UCs	0.0360 $Å^{-1}$
Au@Ag UCs	0.0347 $Å^{-1}$
Number of pixels in CBED patterns:	
Ni@Pt NP (6 nm)	1600×1600
Au@Ag NP (6 nm)	1600×1600
Au@Ag NP (21 nm)	3240×3240
Ni@Pt UCs	576×576
Au@Ag UCs	588×588

Table 1: Parameters for the frozen lattice 4D STEM simulations of the core-shell nanoparticles (NPs) and the corresponding unit cell (UC) simulations with the MULTEM software.

experimental datasets, especially for thicker specimens and signals obtained from lower scattering angles, their contributions will become important.

4. Atom-counting performance

4.1. Ni@Pt core-shell nanoparticle - 6 nm

The performance of the atom-counting methodology is examined for a nanoparticle composed of elements with a large difference in atomic numbers, i.e. Ni (Z^{Ni}=28) and Pt (Z^{Pt}=78). The virtual ADF STEM images obtained from the simulated 4D STEM dataset of the Ni@Pt nanoparticle are shown in Figs. 3(a)-(d) for an electron dose of $10^4 e^-/Å^2$. The ADF STEM images, particularly Figs. 3(b)-(d), reveal a different contrast that allows for a visual differentiation between the Pt-only shell and the mixture of Ni and Pt atoms at the centre.

First, the performance is evaluated for the combination of the two ADF STEM images shown in Figs. 3(a) and (b). To mimic the electron counting noise for realistic measurements, 100 noise realisations for the scattering cross-sections are generated for an electron dose of $10^4 e^-/Å^2$. The number of atoms and their type are then estimated for each of the noise realisations according to Eq. (1). The root mean square error (RMSE) per atomic column is presented in Fig. 3(e) for the total number of atoms, number of Pt and Ni atoms. The average RMSE in a column is summarised in Table 3. However, it is observed that for certain columns, the RMSE is very high, up to 9 atoms, when determining the total number of atoms and the number of Ni atoms. This highlights the complexity of the unscrambling problem leading to a non-unique solution for several atomic columns. In some cases, the addition of a second detector does not fully resolve the overlapping scattering cross-section values.

The probability of error analysis presented in Figs. A.1(a) and (d) suggests that the atom-counting accuracy can be improved when dividing the detector collection region into three detector rings. Therefore, the RMSE per atomic column based on 100 noise realisations is computed for the optimal three detectors (Fig. 3(a),(c) and (d)) and presented in Fig. 3(f). A substantial decrease in the RMSE per atomic column is observed for the number of Ni atoms and, consequently, for the total number of atoms. The average RMSE, presented in Table 3, is consequently also reduced. This result is in agreement with the probability of error analysis provided in Fig. A.1(a) which indicates a clear improvement for an electron dose of $10^4 e^-/Å^2$.

4.2. Au@Ag core-shell nanoparticle - 6 nm

In this section, the performance of the atom-counting methodology is investigated for a Au@Ag core-shell nanoparticle. The difference in atomic number (Z^{Au}=79, Z^{Ag}=47) is lower as compared to the Ni@Pt nanoparticle. The virtual ADF STEM images of the nanoparticle are presented in Figs. 4(a)-(d) for an electron dose of $10^4 e^-/Å^2$. Also here, the contrast varies for the different detector settings. Some detectors clearly reveal the core-shell structures.

First, the combination of two ADF STEM images is examined by utilising the combination of scattering cross-sections estimated from ADF STEM images illustrated in Figs. 4(a) and (b). Also here, the analysis is performed for 100 noise realisations assuming $10^4 e^-/Å^2$. In Fig. 4(e), the RMSE for each atomic

Nanoparticle	Two detectors (mrad)		Three detectors (mrad)		
Ni@Pt (6 nm)	21-30	30-170	21-30	30-34	34-170
Au@Ag (6 nm)	21-27	27-170	21-27	27-37	37-170
Au@Ag (21 nm)	21-71	71-170	21-71	71-101	101-170

Table 2: Optimal detector settings for the combination of two and three ADF STEM images.

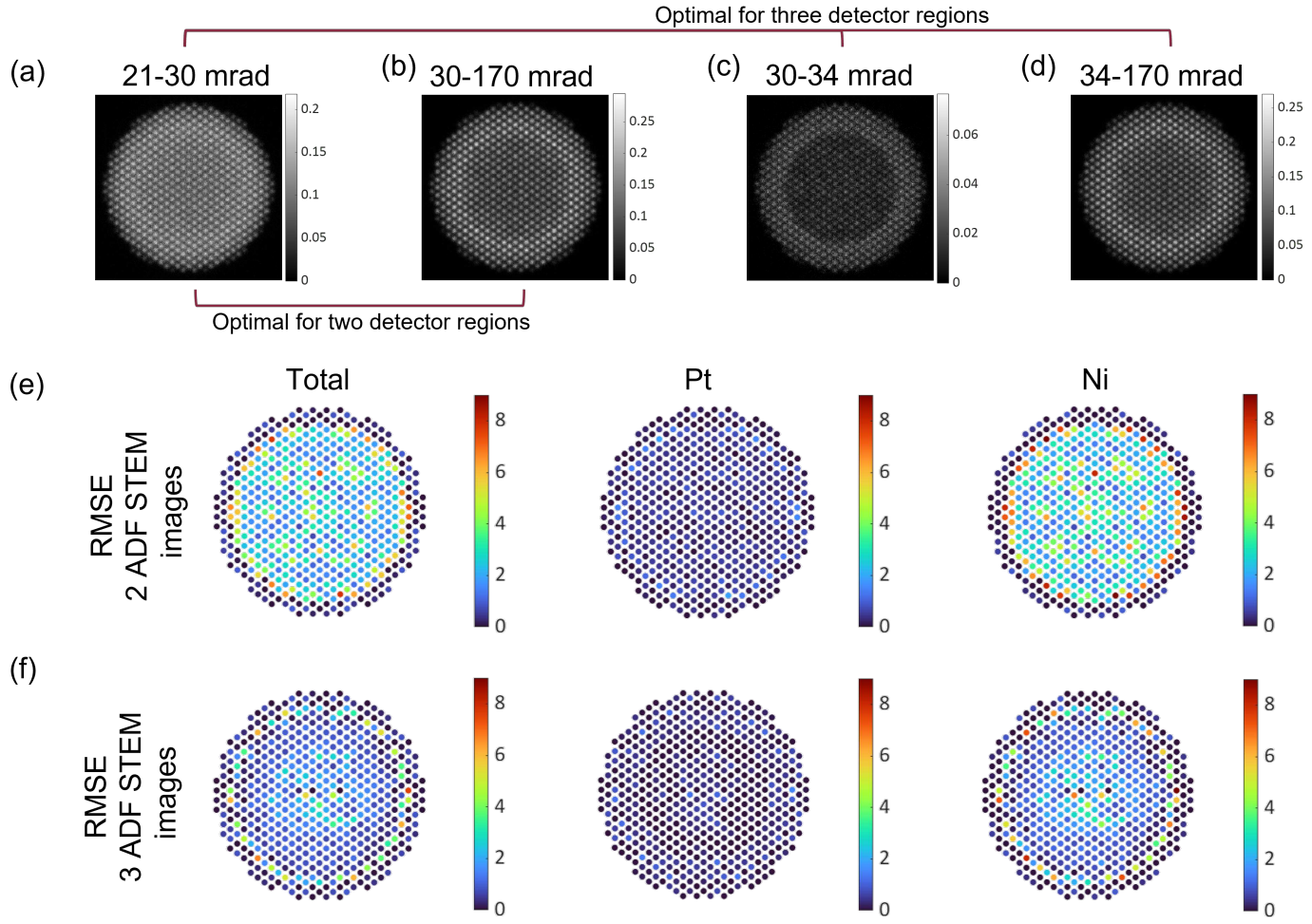

Figure 3: **Ni@Pt nanoparticle (6 nm)**: (a-d) Simulated ADF STEM images of the Ni@Pt nanoparticle including Poisson noise corresponding to an incident electron dose of $10^4 e^-/\text{Å}^2$ with the different detector settings derived from the optimal experiment design study. The RMSE of the atom-counting results for each atomic column based on 100 noise realisations for the combination of (e) two ADF STEM images (a,b) or (f) three ADF STEM images (a,c,d) for the total number of atoms, the number of Pt atoms, and the number of Ni atoms.

column is presented for the atom-counting results obtained using two detector collection ranges. The average RMSE for all atomic columns is given in Table 3.

Next, the atom-counting results obtained from the combination of three ADF STEM images illustrated in Figs. 4(a), (c) and (d) are evaluated. Fig. 4(f) and Table 3, showing the RMSE for each atomic column and the average RMSE respectively, indicate that the combination of three ADF STEM images only yields a minor improvement for this nanoparticle as using a combination of two ADF STEM images already provides accurate estimates. This is in agreement with Fig. A(e), where the benefit is small when comparing the result for two and three detectors.

4.3. Au@Ag core-shell nanoparticle - 21 nm

In section 4.2, we have shown that a combination of only two ADF STEM images provides precise estimation for the composition and thickness of a small Au@Ag core-shell nanoparticle. However, when the thickness of the nanoparticle's atomic columns increases, due to the plenitude of combinations of mixed element atomic columns leading to the same scattering cross-section values, the complexity of the problem further increases. To understand the impact of the nanoparticle size on

Average RMSE	Total number of atoms	Number of core atoms	Number of shell atoms
Ni@Pt (6 nm) -$10^4 e^-/\text{Å}^2$		Ni	Pt
2 detectors	±2.62	±3.01	±0.49
3 detectors	±1.54	±1.78	±0.35
Au@Ag (6 nm) -$10^4 e^-/\text{Å}^2$		Au	Ag
2 detectors	±0.54	±0.97	±1.21
3 detectors	±0.48	±0.82	±1.02
Au@Ag (21 nm) -$10^5 e^-/\text{Å}^2$		Au	Ag
2 detectors	±4.44	±2.81	±7.05
3 detectors	±3.45	±2.20	±5.35
Experimental Au@Ag from [25]		Au	Ag
Combining EDX and HAADF	±3.2	±2.5	±5.6

Table 3: Average RMSE for the atom-counting results.

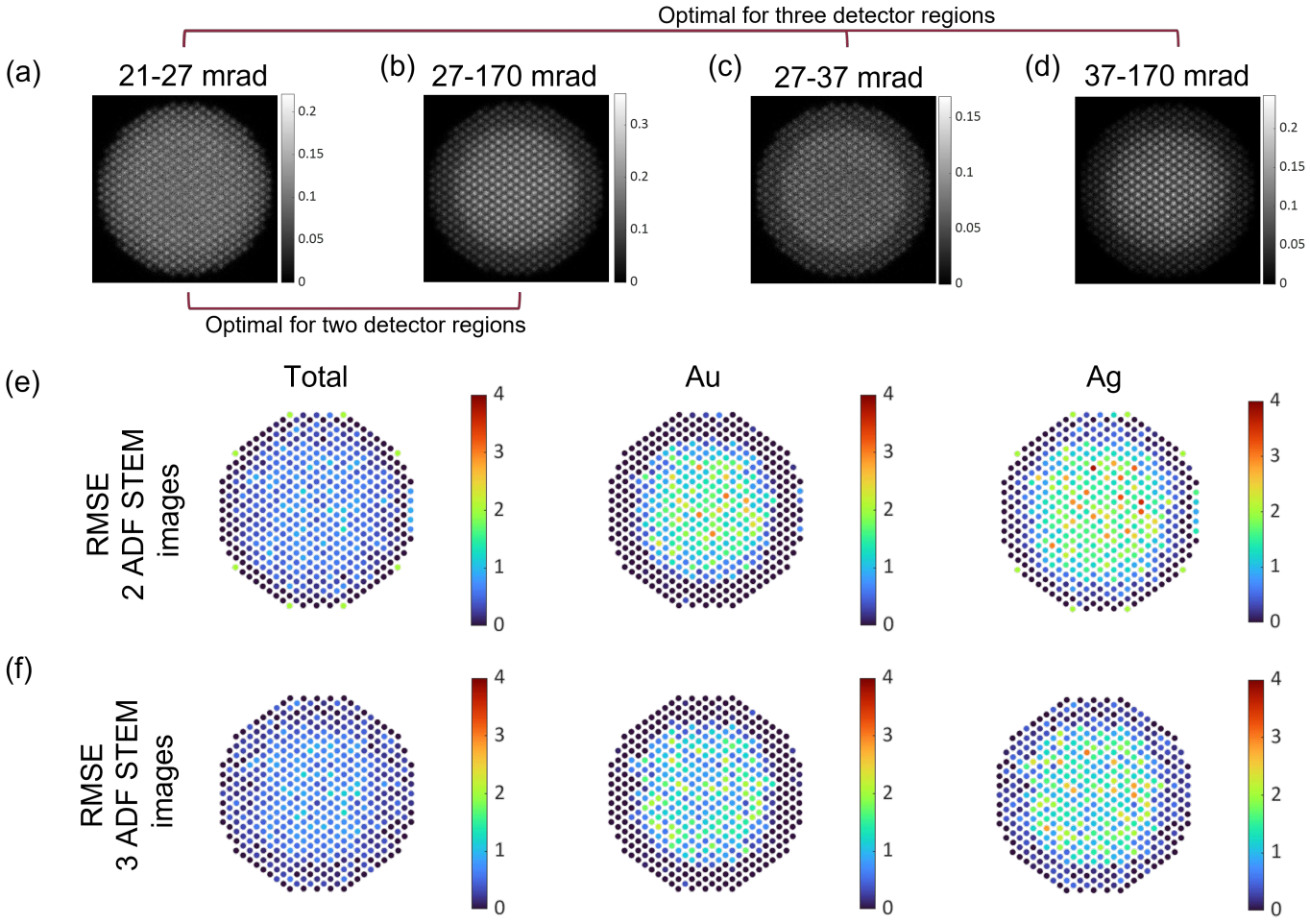

Figure 4: **Au@Ag nanoparticle (6 nm)**: (a-d) Simulated ADF STEM images of the Au@Ag nanoparticle including Poisson noise corresponding to an incident electron dose of $10^4 e^-/\text{Å}^2$ with the different detector settings derived from the optimal experiment design study. The RMSE of the atom-counting results for each atomic column based on 100 noise realisations for the combination of (e) two ADF STEM images (a,b) or (f) three ADF STEM images (a,c,d) for the total number of atoms, the number of Au atoms, and the number of Ag atoms.

the performance of atom-counting methodology and investigate the potential benefits of using more than two ADF STEM detector regions, a spherical core-shell nanoparticle with a thickness varying from 1 up to 80 atoms is considered. The analysis here is limited to the central part of the core-shell nanoparticle which encompasses a segment of the Ag shell with mono-type

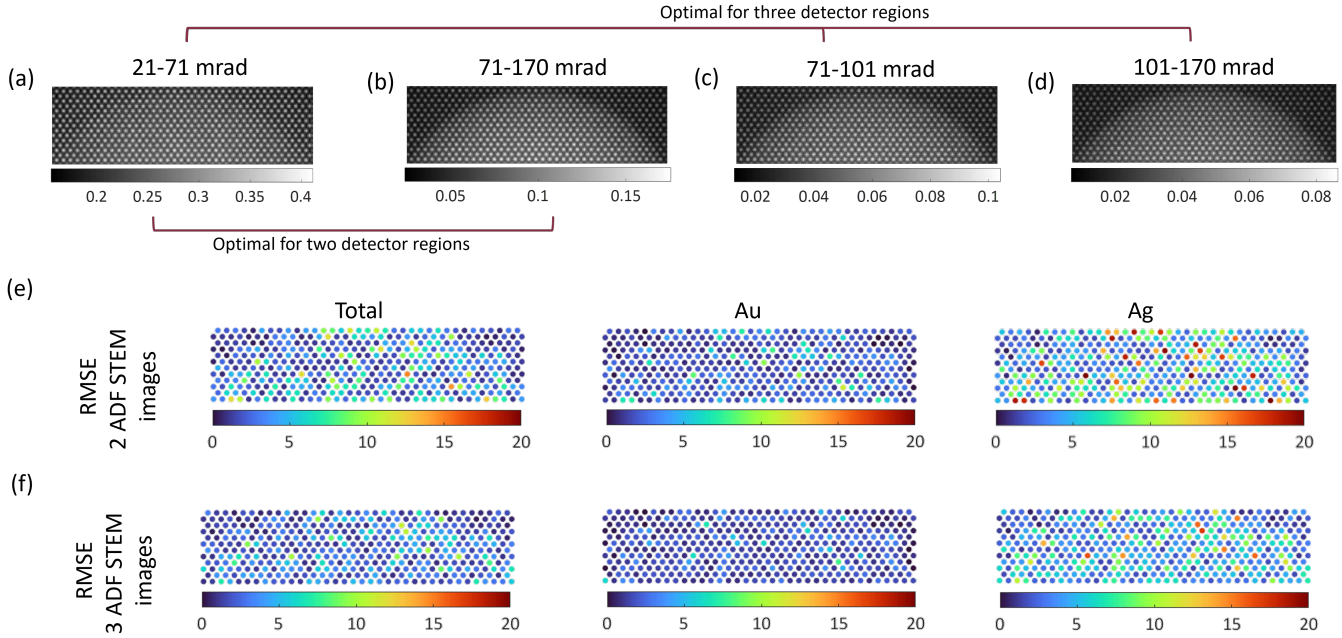

Figure 5: **Au@Ag nanoparticle (21 nm)**: (a-d) Simulated ADF STEM images of the Au@Ag nanoparticle including Poisson noise corresponding to an incident electron dose of $10^5 e^-/\text{Å}^2$ with the different detector settings derived from the optimal experiment design study. The RMSE of the atom-counting results for each atomic column based on 100 noise realisations for the combination of (e) two ADF STEM images (a,b) or (f) three ADF STEM images (a,c,d) for the total number of atoms, the number of Au atoms, and the number of Ag atoms.

Ag atomic columns and a part of the core containing a mixture of Au and Ag atoms. The virtual ADF STEM images obtained from the 4D STEM dataset using the optimal settings are presented in Figs. 5(a)-(d) for an electron dose of $10^5 e^-/\text{Å}^2$. Similar to previous cases, the ADF STEM image generated with the annular detector inner angle just beyond the convergence angle shown in Fig. 5(a) yields the least contrast difference between the core and shell of the nanoparticle. In Fig. 5(e), the RMSE per atomic column based on two detector regions is displayed for the estimated atom counts for each atom type based on 100 noise realisations. The average RMSE is given in Table 3. The obtained errors are acceptable given the thickness of the atomic columns ranging from 60 to 76 atoms.

The probability of error analysis provided in Figs. A.1(c) and (f), suggests a minimal benefit for the large nanoparticle when dividing the annular detector region into three regions instead of two. For completeness, the RMSE per atomic column and the average RMSE is presented in Figure 5(f) and Table 3 respectively, when the combination of three ADF STEM images is used for atom counting. Based on the RMSE values, we do observe an enhancement in the performance of the atom-counting methodology, especially for the lighter Ag atoms. This is in contrast with the probability of error analysis where no benefit was expected with the three detector regions (Fig. A.1(f)). These observations can be related to the fact that the probability of error only refers to the number of incorrectly counted atomic columns and is independent of the magnitude of error made for this wrong assignment. The number of correctly counted atomic columns remains the same for two or three detector regions, while the atom-counting error decreases for three detector areas.

4.4. Dose dependence

The performance of the methodology is further explored under different electron dose conditions as illustrated in Fig. 6. The average RMSE for quantification of each nanoparticle obtained from a combination of two ADF STEM images are compared with those of using three ADF STEM images. The red, blue and yellow colours represent the results for the total number of atoms, the number of atoms of the core and of the shell, respectively. In Fig. 6(a), the average RMSE as a function of dose for the Ni@Pt core-shell nanoparticle is shown. As expected, the RMSE increases when the incident electron dose decreases. The heavier Pt atoms can almost be counted without any error as the electron dose increases. When using two ADF STEM images, the average RMSE is limited to ±2 atoms for the total and the lighter Ni atoms at higher electron dose conditions. At these higher electron doses, the benefit of a third detector becomes evident. Dividing the annular detector region into three parts helps to unscramble the number and types of atoms for the atomic columns of the Ni@Pt nanoparticle which cannot be uniquely determined based on two detector signals.

In Fig. 6(b) the average RMSE per atomic column is shown as a function of dose for the small Au@Ag core-shell nanoparticle. For this case, a smaller error of ±1 is achieved for electron

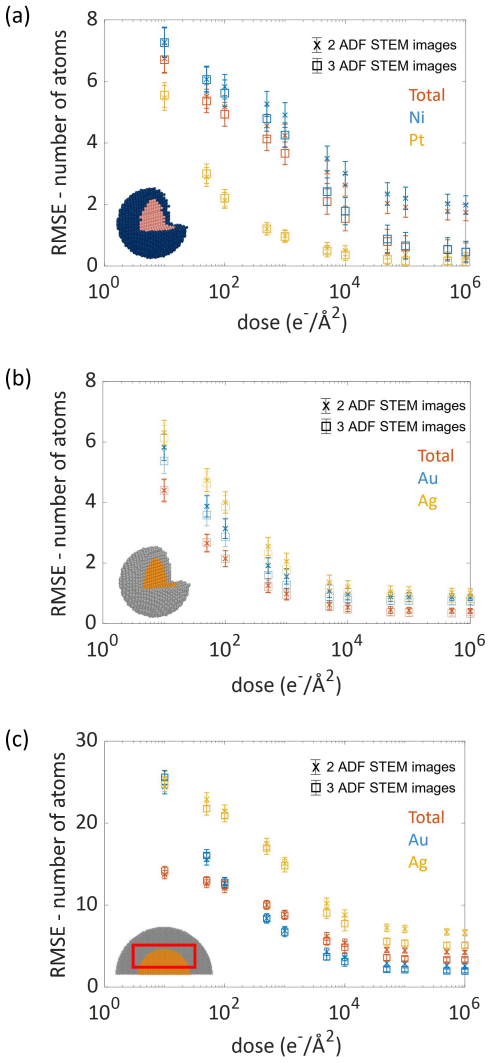

Figure 6: The average RMSE for the total number of atoms (total), the number of atoms of the core (blue) and the number of atoms of the shell (yellow) as a function of electron dose evaluated by using the combination of two (crosses) or three (squares) ADF STEM images for (a) the Ni@Pt core-shell nanoparticle, (b) the Au@Ag core-shell nanoparticle with a diameter of 6 nm and (c) the Au@Ag core-shell nanoparticle with a diameter of 21 nm.

doses larger than $10^4 e^-/\text{Å}^2$ when using both two and three ADF STEM images. The results for the large Au@Ag core-shell nanoparticle, presented in Fig. 6(c), reveal the benefit of a third detector since the average RMSE slightly decreases especially for the number of Ag atoms and the total number of atoms. In general, the values of the average RMSE for unscrambling the number of atoms in this large Au@Ag nanoparticle are similar to the atom-counting errors for a previous study in which the number of Au and Ag atoms were counted for a core-shell Au@Ag nanorod with a similar thickness range based on the combination of EDX and HAADF STEM signals [25]. The average errors of the atom-counting results of that study are also included in Table 3. Compared to the EDX/HAADF approach, the major advantage of the presented method in this paper is the dose efficiency. Here, only one frame with an electron dose of $10^5 e^-/\text{Å}^2$, or even lower, can be acquired, whereas a time series consisting of 12 frames was acquired for the EDX/HAADF experiment. Moreover, for the acquisition of the experimental data in [25], an incident electron dose of around $10^4 e^-/\text{Å}^2$ per frame for the HAADF images was used but a higher dose of around $10^6 e^-/\text{Å}^2$ per frame for the acquisition of the EDX signals was essential to have a sufficient signal-to-noise ratio. Consequently, we propose our new approach as a dose-efficient alternative to using EDX signals, particularly when dealing with beam-sensitive materials.

5. Discussion and conclusion

This study delves into an element-specific atom-counting methodology for heterogeneous nanoparticles based on the combination of multiple ADF STEM images. The method relies on the well-known approach of comparing measured scattering cross-sections from ADF STEM images of a nanoparticle with a set of library values obtained from reference simulations. In this context, the selection of the optimal detector collection regions for the multiple ADF STEM images plays a crucial role. These detector settings yield the most distinct scattering behaviours, enabling the differentiation of various types of atomic columns. Using the optimal detector settings, we successfully applied our methodology to a simulated Ni@Pt and simulated Au@Ag core-shell nanoparticles. The performance of the methodology was evaluated based on the RMSE of the estimated number of atoms for each type of element and the total number of atoms. The average RMSE for the lighter elements is higher than for the heavier elements in the core-shell structure. The scattering cross-sections of atomic columns with light elements might overlap with scattering cross-sections of thinner columns with heavier elements. When limiting the maximal thickness during the assignments of the number of atoms, thicker columns with heavy atoms, can be assigned in a more unique manner. This observation is more pronounced in the Ni@Pt nanoparticle due to the larger atomic number ratio between Ni and Pt compared to Au and Ag, and the heavy Pt atom being the shell element of the core-shell structure. This error can be reduced by increasing the number of segments in the annular detector region. The additional information from a third annular detector collection region, as compared to two collection regions, helps to more uniquely assign the number of atoms in the columns. Concerning the required number of ADF STEM images, the most significant performance improvement is realised when moving from one to two ADF STEM images, while transitioning from two to three images offers lower benefits, as can be seen from the probability of error analysis in Fig. A.1.

Under low electron dose conditions, the error will be mainly determined by the Poisson distributed electron counting noise in the images. When the electron dose increases, the scattering cross-sections can be determined more precisely. The remaining error is then related to the small mismatch between library scattering cross-sections obtained from unit cell simulations and the nanoparticle scattering cross-sections. The dif-

ferent composition and thickness of neighbouring columns influences the exact scattering cross-section values, especially for thicker columns [60]. Because of the high complexity of this atom-counting problem, the neighbouring column effect will contribute to the error. One potential approach to overcome this limitation involves generating library scattering cross-section values that account for the neighbouring column effect. This could be achieved by simulating unit cells composed of different types of atomic columns. However, such an approach would significantly increase the computational cost. Another solution for reducing the errors, which can result in very different column thicknesses for neighbouring columns, is to include a priori knowledge for neighbour-mass relations, where the neighbour mass is constrained based on the average mass of the neighbouring columns [61]. This minimal amount of a priori knowledge might ensure that abrupt continuities are avoided for convex nanoparticles.

In conclusion, this study addresses a challenge that is encountered when attempting atom-counting in heterogeneous nanostructures from a single ADF STEM image. This study demonstrates that this challenge can be addressed through the use of multiple annular detectors. This method is effective for the quantification of heterogeneous nanostructures in a dose-efficient manner, making it a viable alternative for research involving beam-sensitive materials.

Acknowledgements

This work was supported by the European Research Council (Grant 770887 PICOMETRICS to S. Van Aert). The authors acknowledge financial support from the Research Foundation Flanders (FWO, Belgium) through project fundings (G.0346.21N, GOA7723N, and EOS 40007495) and a postdoctoral grant to A. De Backer. S. Van Aert acknowledges funding from the University of Antwerp Research fund (BOF).

A. Probability of error and optimal settings for ADF STEM images

To obtain reliable atom-counting results, one can predict the optimal collection angles of the annular detector. For this purpose, the probability of error was introduced and applied [29, 62]. Using statistical detection theory, the atom-counting problem is then formulated as a statistical hypothesis test, where each hypothesis corresponds to a specific number and type (composition) of atoms in an atomic column. The probability of error corresponds to the probability to choose the wrong hypothesis. In principle, one could also measure the magnitude of the error made by tracking the wrongly assigned hypotheses. However, in this study we use the probability of error to optimise the set of collection angles and we quantify the error for the studied nanoparticles in the main text. To compute the probability of error, 4D STEM simulations of different types of atomic columns are used from which multiple 2D STEM images are generated with varying inner and outer detector angles. The probability of error is computed based on the scattering cross-section values extracted from these virtual 2D STEM images. The results of the probability of error calculations are illustrated for an incident electron dose of $10^4 e^-/\text{Å}^2$ for the Ni@Pt and small Au@Ag core-shell nanoparticles and for an incident electron dose of $10^5 e^-/\text{Å}^2$ for the larger Au@Ag core-shell nanoparticle in Fig. A.1(a)-(c). The probability of error is first computed for two non-overlapping detectors with a shared angle x which is the outer angle for the inner detector (21-x mrad - red detector) and the inner angle for the outer detector (x-170 mrad - blue detector). The optimal settings for the combination of two non-overlapping detectors correspond to the minimum of the yellow curves. To compute the probability of error for three non-overlapping detector settings, one detector is kept equal to the smallest LAADF detector derived from the optimal design for two detectors, since this narrow ring contains only a few mrad of the annular range. The remaining part of the annular detector region is then further divided into two regions similar to the two detector case. The optimal settings for the combination of three non-overlapping detectors correspond to the minimum of the grey curves. Moreover, the evaluation of the probability of error is presented as a function of the incident electron dose in Fig. A.1(d)-(f), presented in the same order as in panels(a)-(c). These figures clearly represent the differences in using two and three annular detector regions. In principle, the probability of error will be further decreased when using even a higher number of annular detectors or ultimately the 4D STEM dataset itself. Nevertheless, we expect the largest benefit from the subdivision into a limited number of detectors considering additional noise contribution from each image [29]. This can also be observed from the fact that the largest decrease in the probability of error is obtained when subdividing the annular range into two regions.

References

[1] P. K. Jain, X. Huang, I. H. El-Sayed, M. A. El-Sayed, Noble metals on the nanoscale: Optical and photothermal properties and some applications in imaging, sensing, biology, and medicine, Accounts of Chemical Research 41 (2008) 1578–1586.

[2] A. H. A. Dabwan, S. Kaneco, H. Katsumata, T. Suzuki, K. Egusa, K. Ohta, Simultaneous removal of trihalomethanes by bimetallic Ag/Zn: kinetics study, Frontiers of Chemical Engineering in China 4 (2010) 322–327.

[3] Y. Han, W. Yan, Bimetallic nickel–iron nanoparticles for groundwater decontamination: Effect of groundwater constituents on surface deactivation, Water Research 66 (2014) 149–159.

[4] S. Shan, J. Luo, N. Kang, J. Wu, W. Zhao, H. Cronk, Y. Zhao, Z. Skeete, J. Li, P. Joseph, S. Yan, C.-J. Zhong, Metallic nanoparticles for catalysis applications, Elsevier, 2015, p. 253–288.

[5] T. Ishida, T. Murayama, A. Taketoshi, M. Haruta, Importance of Size and Contact Structure of Gold Nanoparticles for the Genesis of Unique Catalytic Processes, Chemical Reviews 120 (2019) 464–525.

[6] C. Gao, F. Lyu, Y. Yin, Encapsulated Metal Nanoparticles for Catalysis, Chemical Reviews 121 (2020) 834–881.

[7] M. Cortie, A. McDonagh, Synthesis and optical properties of hybrid and alloy plasmonic nanoparticles, Chemical reviews 111 (2011) 3713–35.

[8] L. Wang, Y. Yamauchi, Strategic Synthesis of Trimetallic Au@Pd@Pt Core-Shell Nanoparticles from Poly(vinylpyrrolidone)-Based Aqueous Solution toward Highly Ative Electrocatalysts, Chemistry of Materials 23 (2011) 2457–2465.

[9] D. Llamosa, M. Ruano, L. Martínez, A. Mayoral, E. Roman, M. García-Hernández, Y. Huttel, The ultimate step towards a tailored engineering

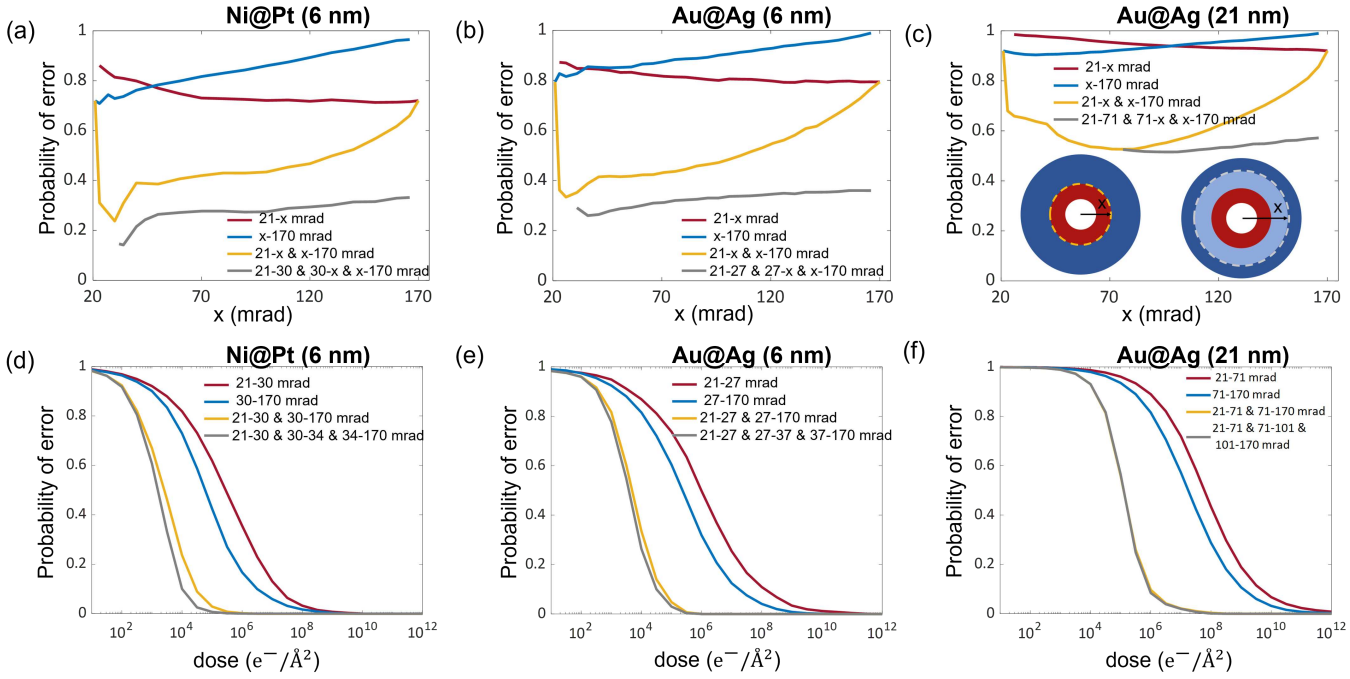

Figure A.1: Probability of error as a function of the outer angle of a single ADF detector with fixed inner angle (red), the inner angle of a single ADF detector with a fixed outer angle (blue), the common angle x for two non-overlapping detectors (yellow) and the common angle x for two independent detectors while the third detector has fixed settings (grey) evaluated for the Ni@Pt core-shell configuration (a), the Au@Ag core-shell configuration (b) with varying thickness from 1 up to 25 atoms for an incident electron dose of $10^4 e^-/\text{Å}^2$, and for a Au@Ag core-shell configuration (c) with varying thickness from 59 up to 81 atoms for an incident electron dose of $10^5 e^-/\text{Å}^2$. The corresponding probability of error as a function of the incident electron dose under the optimised settings for the Ni@Pt core-shell configuration (d), the Au@Ag core-shell configuration (e) with varying thickness from 1 up to 25 atoms, and for the Au@Ag core-shell configuration (f) with varying thickness from 59 up to 81 atoms.

of core@shell and core@shell@shell nanoparticles, Nanoscale 6 (2014) 13483–13486.

[10] F. Zhang, J. Zhu, J.-J. Li, J.-W. Zhao, A promising direct visualization of an Au@Ag nanorod-based colorimetric sensor for trace detection of alpha-fetoprotein, Journal of Materials Chemistry C 3 (2015) 6035–6045.

[11] R. Jiang, S. o. Tung, Z. Tang, L. Li, L. Ding, X. Xi, Y. Liu, L. Zhang, J. Zhang, A review of core-shell nanostructured electrocatalysts for oxygen reduction reaction, Energy Storage Materials 12 (2018) 260–276.

[12] Z. Yan, Y. Zhang, C. Dai, Z. Zhang, M. Zhang, W. Wei, X. Lv, X. Zhao, Porous, thick nitrogen-doped carbon encapsulated large PtNi core-shell nanoparticles for oxygen reduction reaction with extreme stability and activity, Carbon 186 (2022) 36–45.

[13] L. M. Liz-Marzán, Tailoring Surface Plasmons through the Morphology and Assembly of Metal Nanoparticles, Langmuir 22 (2006) 32–41.

[14] H. Zhang, J. Okuni, N. Toshima, One-pot synthesis of Ag–Au bimetallic nanoparticles with Au shell and their high catalytic activity for aerobic glucose oxidation, Journal of Colloid and Interface Science 354 (2011) 131–138.

[15] J. Wu, H. Yang, Platinum-Based Oxygen Reduction Electrocatalysts, Accounts of Chemical Research 46 (2013) 1848–1857.

[16] A. Zaleska-Medynska, M. Marchelek, M. Diak, E. Grabowska, Noble metal-based bimetallic nanoparticles: the effect of the structure on the optical, catalytic and photocatalytic properties, Advances in Colloid and Interface Science 229 (2016) 80–107.

[17] P. D. Nellist, S. J. Pennycook, The Principles and Interpretation of Annular Dark-Field Z-Contrast Imaging, Advances in Imaging and Electron Physics 113 (2000) 147–203.

[18] S. Van Aert, K. J. Batenburg, M. D. Rossell, R. Erni, G. Van Tendeloo, Three-dimensional atomic imaging of crystalline nanoparticles, Nature 470 (2011) 374–377.

[19] P. Kundu, S. Turner, S. Van Aert, N. Ravishankar, G. Van Tendeloo, Atomic Structure of Quantum Gold Nanowires: Quantification of the Lattice Strain, ACS Nano 8 (2014) 599–606.

[20] L. Jones, K. E. MacArthur, V. T. Fauske, A. T. J. van Helvoort, P. D. Nellist, Rapid Estimation of Catalyst Nanoparticle Morphology and Atomic-Coordination by High-Resolution Z-Contrast Electron Microscopy, Nano Letters 14 (2014) 6336–6341.

[21] A. De Backer, L. Jones, I. Lobato, T. Altantzis, B. Goris, P. D. Nellist, S. Bals, S. Van Aert, Three-dimensional atomic models from a single projection using Z-contrast imaging: verification by electron tomography and opportunities, Nanoscale 9 (2017) 8791–8798.

[22] T. Altantzis, I. Lobato, A. De Backer, A. Béché, Y. Zhang, S. Basak, M. Porcu, Q. Xu, A. Sánchez-Iglesias, L. M. Liz-Marzán, G. Van Tendeloo, S. Van Aert, S. Bals, Three-Dimensional Quantification of the Facet evolution of Pt Nanoparticles in a Variable Gaseous Environment, Nano Letters 19 (2019) 477–481.

[23] K. H. W. van den Bos, A. De Backer, G. T. Martinez, N. Winckelmans, S. Bals, P. D. Nellist, S. Aert, Unscrambling mixed elements using high angle annular dark field scanning transmission electron microscopy, Physical Review Letters 116 (2016).

[24] P. Kükelhan, A. Beyer, S. Firoozabadi, T. Hepp, K. Volz, Simultaneous determination of local thickness and composition for ternary III-V semiconductors by aberration-corrected STEM, Ultramicroscopy 201 (2019) 49–57.

[25] A. De Backer, Z. Zhang, K. H. W. van den Bos, E. Bladt, A. Sánchez-Iglesias, L. M. Liz-Marzán, P. D. Nellist, S. Bals, S. Van Aert, Element Specfic Atom Counting at the Atomic Scale by Combining High Angle Annular Dark Field Scanning Transmission Eelectron Microscopy and Energy Dispersive X-ay Spectroscopy, Small Methods (2022) 2200875.

[26] K. Müller-Caspary, O. Oppermann, T. Grieb, F. F. Krause, A. Rosenauer, M. Schowalter, T. Mehrtens, A. Beyer, K. Volz, P. Potapov, Materials characterisation by angle-resolved scanning transmission electron microscopy, Scientific Reports 6 (2016) 37146.

[27] J. Y. Zhang, J. Hwang, B. J. Isaac, S. Stemmer, Variable-angle high-angle

annular dark-field imaging : application to three-dimensional dopant atom profiling, Scientific Reports 5 (2015) 12419.
[28] D. Şentürk, C. P. Yu, A. De Backer, V. Aert, Atom counting from a combination of two ADF STEM images, Ultramicroscopy 255 (2024) 113859.
[29] D. G. Şentürk, A. De Backer, T. Friedrich, S. Van Aert, Optimal experiment design for element specific atom counting using multiple annular dark field scanning transmission electron microscopy detectors, Ultramicroscopy 242 (2022) 113626.
[30] N. Shibata, Y. Kohno, S. D. Findlay, H. Sawada, Y. Kondo, Y. Ikuhara, New area detector for atomic-resolution scanning transmission electron microscopy, Journal of Electron Microscopy 59 (2010) 473–479.
[31] A. R. Faruqi, G. McMullan, Direct imaging detectors for electron microscopy, Nuclear Instruments & Methods in Physics Research, Section A: Accelerators, Spectrometers, Detectors, and Associated Equipment 878 (2018) 180–190.
[32] H. Yang, R. N. Rutte, L. Jones, M. Simson, R. Sagawa, H. Ryll, M. Huth, S. J. Pennycook, M. L. H. Green, H. Soltau, Y. Kondo, B. G. Davis, P. D. Nellist, Simultaneous atomic-resolution electron ptychography and Z-contrast imaging of light and heavy elements in complex nanostructures, Nature Communications 7 (2016) 2532.
[33] C. Ophus, Four-Dimensional Scanning Transmission Electron Microscopy 4D-STEM: From Scanning Nanodiffraction to Ptychography and Beyond, Microscopy and Microanalysis 25 (2019) 563–582.
[34] Y. Wen, C. Ophus, C. S. Allen, S. Fang, J. Chen, E. Kaxiras, A. I. Kirkland, J. H. Warner, Simultaneous Identification of Low and High Atomic Number Atoms in Monolayer 2D Materials Using 4D Scanning Transmission Electron Microscopy, Nano Letters 19 (2019) 6482–6491.
[35] J. LeBeau, S. Stemmer, Experimental quantification of annular dark-field images in scanning transmission electron microscopy, Ultramicroscopy 108 (2008) 1653–8.
[36] A. Rosenauer, K. Gries, K. Müller, A. Pretorius, M. Schowalter, A. Avramescu, K. Engl, S. Lutgen, Measurement of specimen thickness and composition in $Al_xGa_{1-x}N$/GaN using high-angle annular dark field images, Ultramicroscopy 109 (2009) 1171—1182.
[37] T. Grieb, K. Müller, R. Fritz, M. Schowalter, N. Neugebohrn, N. Knaub, K. Volz, A. Rosenauer, Determination of the chemical composition of GaNAs using STEM HAADF imaging and STEM strain state analysis, Ultramicroscopy 117 (2012) 15–23.
[38] H. Kauko, T. Grieb, R. Bjørge, M. Schowalter, A. Munshi, H. Weman, A. Rosenauer, A. van Helvoort, Compositional characterization of GaAs/GaAsSb nanowires by quantitative HAADF-STEM, Micron 44 (2013) 254–260.
[39] A. Beyer, L. Duschek, J. Belz, J. O. Oelerich, K. Jandieri, K. Volz, Surface relaxation of strained Ga(P,As)/GaP heterostructures investigated by HAADF STEM, Journal of Microscopy 268 (2017) 239–247.
[40] L. Duschek, P. Kükelhan, A. Beyer, S. Firoozabadi, J. Oelerich, C. Fuchs, W. Stolz, A. Ballabio, G. Isella, K. Volz, Composition determination of semiconductor alloys towards atomic accuracy by HAADF-STEM, Ultramicroscopy 200 (2019) 84–96.
[41] J. Barthel, M. Cattaneo, B. G. Mendis, S. D. Findlay, L. J. Allen, Angular dependence of fast-electron scattering from materials, Physical Review B 101 (2020).
[42] A. Beyer, F. F. Krause, H. L. Robert, S. Firoozabadi, T. Grieb, P. Kükelhan, D. Heimes, M. Schowalter, K. Müller-Caspary, A. Rosenauer, K. Volz, Influence of plasmon excitations on atomic-resolution quantitative 4D scanning transmission electron microscopy, Scientific Reports 10 (2020) 17890.
[43] K. Nakazawa, K. Mitsuishi, K. Shibata, S. Amma, T. Mizoguchi, Local thickness and composition measurements from scanning convergent-beam electron diffraction of a binary non-crystalline material obtained by a pixelated detector, Ultramicroscopy 217 (2020) 113077.
[44] E. Thronsen, T. Bergh, T. Thorsen, E. Christiansen, J. Frafjord, P. Crout, A. van Helvoort, P. Midgley, R. Holmestad, Scanning precession electron diffraction data analysis approaches for phase mapping of precipitates in aluminium alloys, Ultramicroscopy 255 (2024) 113861.
[45] S. Van Aert, J. Verbeeck, R. Erni, S. Bals, M. Luysberg, D. V. Dyck, G. V. Tendeloo, Quantitative atomic resolution mapping using high-angle annular dark field scanning transmission electron microscopy, Ultramicroscopy 109 (2009) 1236–1244.
[46] H. E, K. E. MacArthur, T. J. Pennycook, E. Okunishi, A. J. D'Alfonso, N. R. Lugg, L. J. Allen, P. D. Nellist, Probe integrated scattering cross sections in the analysis of atomic resolution HAADF STEM images, Ultramicroscopy 133 (2013) 109–119.
[47] G. T. Martinez, A. Rosenauer, A. De Backer, J. Verbeeck, S. Van Aert, Quantitative composition determination at the atomic level using model-based high-angle annular dark field scanning transmission electron microscopy, Ultramicroscopy 137 (2014) 12–19.
[48] K. E. MacArthur, A. J. D'Alfonso, D. Ozkaya, L. J. Allen, P. D. Nellist, Optimal ADF STEM imaging parameters for tilt-robust image quantification, Ultramicroscopy 156 (2015) 1–8.
[49] A. Rosenauer, T. Mehrtens, K. Müller, K. Gries, M. Schowalter, P. Venkata Satyam, S. Bley, C. Tessarek, D. Hommel, K. Sebald, M. Seyfried, J. Gutowski, A. Avramescu, K. Engl, S. Lutgen, Composition mapping in InGaN by scanning transmission electron microscopy, Ultramicroscopy 111 (2011) 1316–1327.
[50] S. Van Aert, A. De Backer, G. T. Martinez, B. Goris, S. Bals, G. Van Tendeloo, Procedure to count atoms with trustworthy single-atom sensitivity, Physical Review B 87 (2013).
[51] S. Van Aert, A. De Backer, G. T. Martinez, B. Goris, S. Bals, G. Van Tendeloo, Atom counting in HAADF STEM using a statistical model-based approach: Methodology, possibilities, and inherent limitations, Ultramicroscopy 134 (2013) 23–33.
[52] A. De Backer, K. H. W. van den Bos, W. Van den Broek, J. Sijbers, S. Van Aert, StatSTEM: An efficient approach for accurate and precise model-based quantification of atomic resolution electron microscopy images, Ultramicroscopy 171 (2016) 104–116.
[53] K. H. W. van den Bos, L. Janssens, A. De Backer, P. D. Nellist, S. Van Aert, The atomic lensing model: New opportunities for atom-by-atom metrology of heterogeneous nanomaterials, Ultramicroscopy 203 (2019) 155–162.
[54] I. Lobato, D. Van Dyck, MULTEM: A new multislice program to perform accurate and fast electron diffraction and imaging simulation using Graphics Processing Units with CUDA, Ultramicroscopy 156 (2015) 9–17.
[55] H. X. Gao, L.-M. Peng, Parameterization of the temperature dependence of the Debye-Waller factors, Acta Crystallographica Section A 55 (1999) 926–932.
[56] V. Grillo, E. Carlino, F. Glas, Influence of the static atomic displacement on atomic resolution Z-contrast imaging, Physical Review B 77 (2008).
[57] V. Grillo, K. Mueller, K. Volz, F. Glas, T. Grieb, A. Rosenauer, Strain, composition and disorder in ADF imaging of semiconductors, Journal of Physics: Conference Series 326 (2011) 012006.
[58] T. Grieb, F. F. Krause, K. Müller-Caspary, S. Firoozabadi, C. Mahr, M. Schowalter, A. Beyer, O. Oppermann, K. Volz, A. Rosenauer, Angle-resolved STEM using an iris aperture: Scattering contributions and sources of error for the quantitative analysis in Si, Ultramicroscopy 221 (2021) 113175.
[59] H. L. Robert, B. Diederichs, K. Müller-Caspary, Contribution of multiple plasmon scattering in low-angle electron diffraction investigated by energy-filtered atomically resolved 4D-STEM, Applied Physics Letters 121 (2022) 213502.
[60] Z. Zhang, I. Lobato, A. De Backer, S. Van Aert, P. D. Nellist, Fast generation of calculated ADF-EDX scattering cross-sections under channelling conditions, Ultramicroscopy 246 (2023) 113671.
[61] A. De Backer, S. Van Aert, C. Faes, E. Arslan Irmak, P. D. Nellist, L. Jones, Experimental reconstructions of 3D atomic structures from electron microscopy images using a Bayesian genetic algorithm, npj Computational Materials 8 (2022) 215.
[62] A. De Backer, A. De wael, J. Gonnissen, S. Van Aert, Optimal experimental design for nano-particle atom-counting from high-resolution STEM images, Ultramicroscopy 151 (2015) 46–55.